

# Strong Activity Changes Observable during the First Pretreatment Cycles of Trimetallic PtNiMo/C Catalysts

Bilal Danisman,<sup>[a]</sup> Gui-Rong Zhang,<sup>[a, b]</sup> Adrian F. Baumunk,<sup>[a]</sup> Juntao Yang,<sup>[c]</sup> Olaf Brummel,<sup>[c]</sup> Philipp Darge,<sup>[d]</sup> Karl J. J. Mayrhofer,<sup>[d]</sup> Jörg Libuda,<sup>[c]</sup> Marc Ledendecker,<sup>[a, e]</sup> and Bastian J. M. Etzold\*<sup>[a]</sup>

Pt-based alloy catalysts supported on carbon are commonly characterized for oxygen reduction reaction (ORR) activity using the rotating disk electrode technique (RDE). Within this study, we show exemplarily for PtNiMo/C catalysts that the applied pretreatment influences strongly the determined activity. The classically employed descriptor of unchanged cyclic voltammetry response is insufficient to portrait completed surface restructuring, and gives an incorrect impression that stable activity can be determined. This might be one of the reasons for the strongly deviating activities reported in literature.

Following the changes in activity during pretreatment also with in-situ FTIR and online dissolution measurements gives insights to an up to now largely overseen high activity of the trimetallic catalysts. A maximum activity of  $0.57 \text{ mA cm}_{\text{Pt}}^{-2}$  at  $0.95 V_{\text{RHE}}$  is reached quickly during the first six cycles and decreases slowly subsequently. The maximum activity and change of activity over the cycle number is affected by the scan rate and electrolyte refreshing, while the gas atmosphere plays only a minor role. This exemplary study might be important for Pt alloy catalysts in general.

## Introduction

Platinum-based catalysts are state of the art oxygen reduction reaction (ORR) catalysts used in proton-exchanged membrane fuel cells (PEMFC).<sup>[1,2]</sup> The sluggish kinetics on the cathode as well as the poor stability at potentials above  $1.0 V_{\text{RHE}}$  motivates to improve catalysts in activity and durability.<sup>[1–4]</sup> From a structural point of view, Pt(111) facets were identified to belong to the most active surfaces.<sup>[5]</sup> In literature, various strategies to

increase the specific activity have been reported ranging from alloying with transition metals (e.g. Ni, Fe, Co) to induce lattice strain,<sup>[6]</sup> nano structuring,<sup>[7–9]</sup> size optimization,<sup>[10]</sup> adjusting surface composition,<sup>[9–12]</sup> implementing defect sites and concave structures.<sup>[15,16]</sup> Strasser and co-workers reported for PtNiMo catalyst the synthesis of octahedral shaped nanoparticles with Pt-rich edges and vertices and Ni-rich facets, while Mo acts as a surface dopant and is located on the Pt-rich edges and vertices.<sup>[17]</sup>

Despite these achievements in increasing the activity, the stability of alloy catalysts remains a challenge above  $0.95 V_{\text{RHE}}$ .<sup>[18]</sup> One example are octahedral shaped PtNi nanoparticles with a high share of (111)-facets.<sup>[18,19]</sup> Here, metal leaching such as Ni at conditions up to  $0.95 V_{\text{RHE}}$  and additional shape loss with declining electrochemical active surface area (ECSA) especially due to Pt oxidation over  $0.95 V_{\text{RHE}}$  are the main causes for the observed decreasing activity.<sup>[18,19]</sup> It was reported that the stability can be increased, when alloying a third metal (e.g. Mo,<sup>[17,20]</sup> Co,<sup>[21]</sup> Rh<sup>[22]</sup>). For instance, we recently also demonstrated the degradation behavior of trimetallic PtNiMo/C catalysts showing an increased stability, but using a scanning flow cell inductively coupled plasma mass spectrometry (SFC-ICP-MS) analysis, which proofs ongoing dissolution of transient metals (i.e. Ni, Mo) over time.<sup>[23,19]</sup>

The consideration of the dynamics of such alloy and nanostructure catalysts originated from the studies of polycrystalline alloy films of  $\text{Pt}_3\text{M}$  (M = transition metals), where a thermal annealing under ultrahigh vacuum at 1000 K leads to an enrichment of Pt atoms at the first layer due to segregation, forming the so-called “Pt-skin” structure.<sup>[24,25]</sup> Studies of a single-crystal  $\text{Pt}_3\text{Ni}$  surface from Markovic and co-workers confirmed the formation of a Pt-skin on the surface atomic layer, where the first and third layer are Pt rich and the second layer is Ni rich.<sup>[7]</sup> This arrangement favors the electronic structure by the


[a] B. Danisman, Prof. Dr. G.-R. Zhang, A. F. Baumunk, Prof. Dr. M. Ledendecker, Prof. Dr.-Ing. B. J. M. Etzold  
Department of Chemistry, Ernst-Berl-Institute for Technical and Macromolecular Chemistry  
Technical University of Darmstadt  
64287 Darmstadt (Germany)  
E-mail: bastian.etzold@tu-darmstadt.de  
Homepage: www.etzoldlab.de


[b] Prof. Dr. G.-R. Zhang  
School of Chemical Engineering and Technology  
Tiangong University  
BinShuiXi Road 399, Tianjin 300387 (China)

[c] J. Yang, Dr. O. Brummel, Prof. Dr. J. Libuda  
Erlangen Center for Interface Research and Catalysis  
FAU Erlangen-Nürnberg  
Egerlandstr. 3, 91058 Erlangen (Germany)

[d] P. Darge, Prof. Dr. K. J. J. Mayrhofer  
Forschungszentrum Jülich GmbH  
Helmholtz-Institute Erlangen-Nürnberg for Renewable Energy (IEK-11)  
Cauerstr. 1, 91058 Erlangen (Germany)

[e] Prof. Dr. M. Ledendecker  
Department of Sustainable Energy Materials  
Campus Straubing for Biotechnology and Sustainability  
Technical University of Munich  
94315 Straubing (Germany)

 Supporting Information for this article is available on the WWW under <https://doi.org/10.1002/celec.202300109>

 © 2023 The Authors. ChemElectroChem published by Wiley-VCH GmbH. This is an open access article under the terms of the Creative Commons Attribution License, which permits use, distribution and reproduction in any medium, provided the original work is properly cited.

contraction of Pt surface atoms with increased surface stability.<sup>[7]</sup>

These dynamics of catalyst properties bring special challenges in assessing the activity and pre-activation/conditioning procedures of the catalysts that are applied in classical RDE testing to get the catalyst to a first “equilibrated” initial state. Already for Pt/C catalysts, the importance for a catalyst pretreatment in order to reach a steady state was pointed out.<sup>[26–28]</sup> Steady state or “equilibrated” initial state was thereby defined as no further changes in the Pt-characteristics of the  $H_{UPD}$  and Pt-oxidation/reduction region were observed. For alloy catalysts, the changes in ECSA can be attributed to the leaching process of transient metals (i.e. Ni, Mo) and thus exposing new Pt-sites due to morphological changes. Additionally, pretreatment was found to reduce ORR overpotentials.<sup>[20]</sup>

While the ECSA change during catalyst restructuring within the pretreatment procedure has been reported,<sup>[17,20]</sup> no information is available on the alteration in catalytic performance during pretreatment which is the scope of this study. In order to do so, a literature known, octahedral shaped PtNiMo/C alloy catalyst was employed.<sup>[29,20]</sup> Subsequently, the surface area and surface- and mass-specific activity was studied and related to the employed pretreatment. This includes variation of atmosphere ( $N_2/O_2$ ), scan-rate ( $20/500\text{ mVs}^{-1}$ ), cycle-number and exchange of electrolyte. Unprecedented high activities can be obtained between five and fifteen ORR-cycles. Interestingly, non-linear activity changes take place during pretreatment while the ECSA remains constant.

## Results and Discussion

### Identifying regime of interest for initial activity changes

First, the change in ECSA and activity for the employed catalyst during pretreatment conditions at a scan-rate of  $500\text{ mVs}^{-1}$  in  $N_2$  saturated  $0.1\text{ M HClO}_4$  and increasing cycle numbers were recorded (Figure 1). Additionally, 800 cyclic voltammetry (CV) curves were recorded and slow scanning CVs and ORR polarization curves with an anodic linear sweep voltammetry (LSV) at  $20\text{ mVs}^{-1}$  and 1600 rpm determined in the potential range of  $0.05\text{--}1.20\text{ V}_{RHE}$  without additional pretreatment and after 6, 50, 100, 150, 200, 300, 400, 600, 800 cycles. Prior to the polarization curves, the electrolyte was exchanged. The development of the CVs and specific activities for different conditioning cycle numbers are given in Figure 1. The characteristic peaks such as hydrogen adsorption/desorption ( $0.05$  to  $0.42\text{ V}_{RHE}$ ) and Pt oxidation/reduction ( $0.47$  to  $1.09\text{ V}_{RHE}$ ) are suppressed at the beginning and develop with continuing cycling resulting in a steady state CV curve (Figure 1a). The current density for hydrogen adsorption and desorption increases, where latter shows a change of the charge density from  $190$  to  $890\text{ }\mu\text{Ccm}_{Pt}^{-2}$ . Furthermore,  $OH^*/O^*$  adsorption, Pt oxidation and reduction peaks develop and charge densities of  $360$  and  $1080\text{ }\mu\text{Ccm}_{Pt}^{-2}$  are obtained, respectively. The ECSA changes throughout increasing cycle numbers between  $41\text{--}48\text{ m}^2\text{g}_{Pt}^{-1}$  (Figure 1b). A fast increase of the ECSA within the first sixth

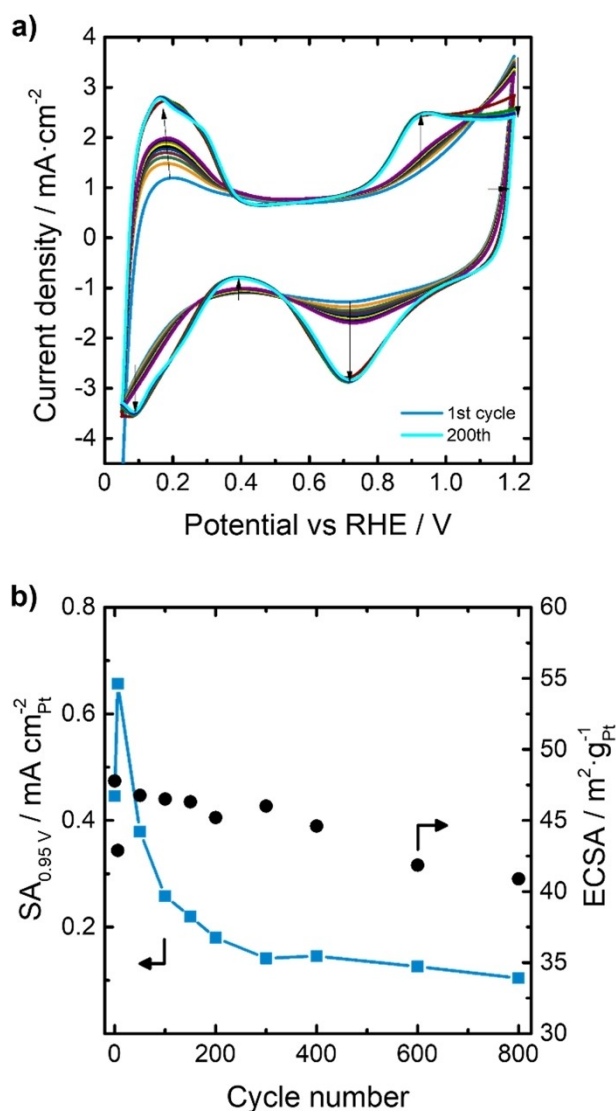


**Figure 1.** a) Development of a cyclic voltammetry curve in  $N_2$  during 200 conditioning cycles at  $500\text{ mVs}^{-1}$ . b) Specific activities at  $0.95\text{ V}_{RHE}$  in  $O_2$  and ECSA development throughout increasing conditioning cycle numbers from initial to 800 cycles for PtNiMo/C. Potential range:  $0.05\text{--}1.20\text{ V}_{RHE}$ . CV/ORR at  $20\text{ mVs}^{-1}$ , ORR with rotation at 1600 rpm in  $N_2/O_2$ -saturated  $0.1\text{ M HClO}_4$ .

conditioning cycles can be seen, followed by a steady slow decrease from the 50<sup>th</sup> to 800<sup>th</sup> cycle. As we look closer into the resulting activities for different cycle numbers at  $0.95\text{ V}_{RHE}$  (Figure 1b), we observe varying activities between 0–800 cycles. Low cycle numbers up to 100 cycles show the highest volatility, which vary between  $0.26\text{ mAcm}_{Pt}^{-2}$  (after 100 cycles) and an activity of  $0.66\text{ mAcm}_{Pt}^{-2}$  (or  $6.06\text{ mAcm}_{Pt}^{-2}$  at  $0.90\text{ V}_{RHE}$  in Figure S2 in Supporting Information) after 6 cycles approaching the high activities reported from Huang et al.<sup>[29]</sup> Even without any prior conditioning, the first measurement yielded a high specific activity (SA) of  $0.45\text{ mAcm}_{Pt}^{-2}$ , demonstrating the enhanced activity of the trimetallic catalyst. This sharp increase in the first six cycles continues with an equally sharp decrease within 100 cycles and an ongoing flattened decline from 200–800 cycles upon further conditioning. In this, the SA at  $0.95\text{ V}_{RHE}$

continually varies between 0.18–0.10 mA cm<sub>Pt</sub><sup>-2</sup>. The dynamic changes in the trimetallic catalyst result from different active states induced by the morphological changes due to the leaching processes of transition metals. Overall the CV data demonstrates that while the ECSA determined for each conditioning cycle number only differs slightly, the SA varies significantly and passes a pronounced maximum (0.66 mA cm<sub>Pt</sub><sup>-2</sup>). As region of interest for further studies, the very first cycles showing the maximum were chosen.

### Cycling either in N<sub>2</sub> or O<sub>2</sub> saturated electrolyte

To gain more insights to the initial sharp activity increase and following decrease, the initial pretreatment CV cycles were carried out at a lower scanning rate (20 mV s<sup>-1</sup>). This allows to record changes in the hydrogen adsorption, H<sub>upd</sub> stripping, Pt oxidation, Pt reduction and double layer regime for every cycle. The CV curves recorded in N<sub>2</sub> saturated 0.1 M HClO<sub>4</sub> at 20 mV s<sup>-1</sup> and calculated ECSA, as well as the charge of Pt oxide reduction (Q<sub>Pt-Red</sub>) are given in Figure 2. During this cycling in N<sub>2</sub>, several changes of the CV become obvious. The double layer region between 0.35–0.60 V<sub>RHE</sub> shows an ongoing minor decrease of capacitance. The faradaic oxidation currents above 1.00 V<sub>RHE</sub> declining over time, which could be mainly attributed to the removal of organics on the carbon support, impurities, and ligands from the synthesis. Consequently, within the potential range of hydrogen adsorption/desorption (0.05–0.40 V<sub>RHE</sub>) an increase of the hydrogen adsorption is seen and the calculated ECSA increases from 35 to 42 m<sup>2</sup> g<sub>Pt</sub><sup>-1</sup> until the 9<sup>th</sup> cycle and remains approximately constant with successive cycling. Increasing faradaic currents are also visible within the range of Pt surface oxidation at a higher potential range of 0.80–1.00 V<sub>RHE</sub> and Pt oxide reduction (0.40–0.95 V<sub>RHE</sub>). The charge of Pt reduction (Q<sub>Pt-Red</sub>) increases strongly during the first 15 cycles and remains constant after 20 cycles.

While the observed changes in charge capacity agree qualitatively with literature,<sup>[30,31–34]</sup> a detailed assessment of specific activity and cycle numbers has, to be best of the authors knowledge, not been reported. In order to do so, a pretreatment procedure was applied where the potential was swept from 0.05 to 1.20 V<sub>RHE</sub> with a scan rate of 20 mV s<sup>-1</sup> under forced convection at 1600 rpm and O<sub>2</sub> saturated HClO<sub>4</sub>. The surface specific and mass specific activity (MSA) was determined while no information on ECSA changes is available. Here, after the pretreatment in O<sub>2</sub> an ECSA was determined in N<sub>2</sub> at the end of the cycling allowing to calculate “SA<sub>CVend</sub>”. As the ECSA changes are smaller (approximately 20%) compared to the changes in activity (>50%), the SA/MSA is calculated to allow an approximate comparison with literature values independent of the nanoparticle structure (Figure 3). The calculated SA and MSA (Figure 3b) develop dynamically, with a sharp increase in SA from 0.24 mA cm<sub>Pt</sub><sup>-2</sup> at the first polarization curve (without any pretreatment) to a maximum of 0.49 mA cm<sub>Pt</sub><sup>-2</sup> after eight ORR-polarizations. An explanation may lay in the electrochemical cleaning of the catalyst and the associated transition metal leaching exposing Pt active sites

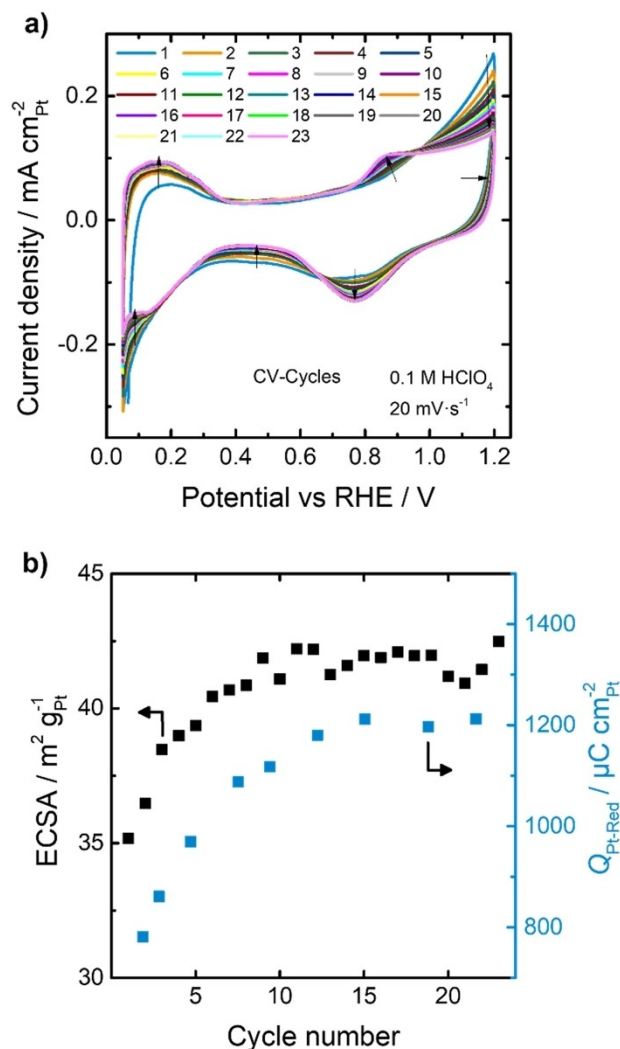


**Figure 2.** a) Development of cyclic voltammetry curves with pretreatment. b) ECSA and Q<sub>Pt-Red</sub> development of PtNiMo/C. Recorded in N<sub>2</sub>-saturated 0.1 M HClO<sub>4</sub> electrolyte in potential range of 0.05–1.20 V<sub>RHE</sub> and scan-rate of 20 mV s<sup>-1</sup>.

and therefore increasing the specific activity. Beside this, the removal of surface contaminations and impurities, such as oxygenated species, carbon overlayers from Ketjenblack as well as surfactants and solvents from synthesis might also contribute to the observed increase in surface specific activity.<sup>[29,35]</sup> Furthermore, the segregation behavior of Pt to the outer surface at Pt-alloy catalysts can result in the formation of a stabilizing Pt-overlayer surface.<sup>[7]</sup> A possible increase in porosity can be excluded based on the same surface area evolution and as the CV cycling shown in Figure 2a indicates minor changes.<sup>[36,37]</sup>

The maximum in SA<sub>CVend</sub> illustrates an “ideal” morphological change of the octahedral nanoparticle with probably the highest availability of highly active sites. Further cycling, however, results in a moderate decrease in SA. This could be attributed to ongoing morphological changes and loss of 111-facets as well as the leaching of Ni and Mo.<sup>[7,23]</sup> Additionally

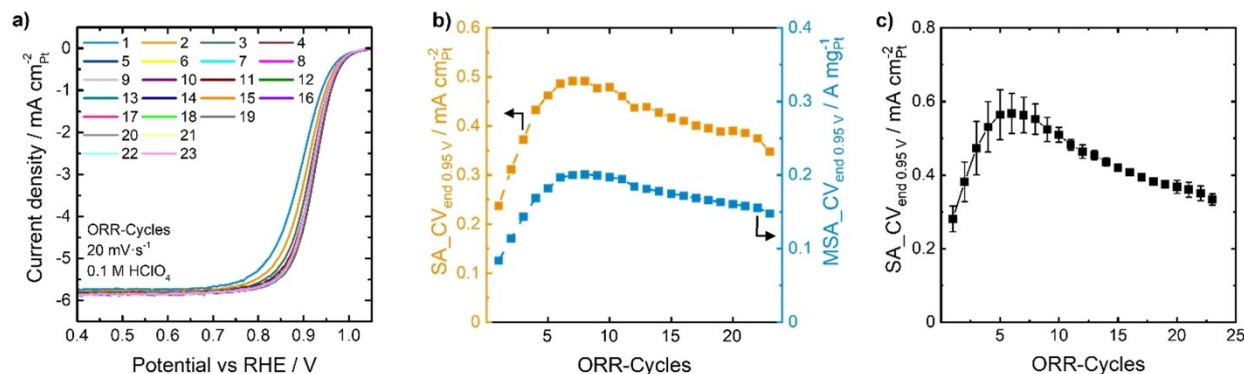


**Figure 3.** a) Development of polarization curve during pretreatment. b)  $SA_{CV_{end}}$  and  $MSA_{CV_{end}}$  progress in dependence of ORR cycle numbers at  $0.95 V_{RHE}$ . c) Average  $SA_{CV_{end}}$  screening values from different catalyst inks of PtNiMo/C. Recorded in  $O_2$ -saturated  $0.1 M HClO_4$  electrolyte (potential range:  $0.05$ – $1.20 V_{RHE}$ ; scan-rate:  $20 mV s^{-1}$  with rotation at  $1600 rpm$ ).

during cycling, impurities can accumulate on the electrode and result in lower observed SA.<sup>[38]</sup>

Figure 3c gives insights into the reproducibility. While the initial SA development show higher deviations (6–15%) up to the 9th ORR-cycle, a continuous cycling leads to a converge of the average SA result. The deviations in absolute activity might stem not only from the usual aspects in RDE testing, such as ink preparation and electrode coverage homogeneity,<sup>[38,39]</sup> but also from the undefined starting point (Figure S3b in Supporting Information). No additional pretreatment was carried out during these studies, thus an equilibration of the catalyst before starting the experiment is missing. In general, the maximum in SA is reached within five and eight ORR-cycles. Thereby, the SA increases approximately by a factor of 2.1 and up to a value of  $0.57 mA cm_{Pt}^{-2}$ .

As the cyclic voltammetry measurements result in significant ECSA,  $Q_{Pt-Red}$  and SA/MSA development for the trimetallic PtNiMo/C catalyst, a comparison to a single Pt/C catalyst is performed to identify the particular role of the transition metals (Ni, Mo). Therefore, a CV measurement is carried out with a single Pt/C catalyst (HiSpec-3000) in the same potential range of  $0.5$ – $1.20 V_{RHE}$  at  $20 mVs^{-1}$  in a  $N_2$  saturated  $0.1 M HClO_4$  solution and is given Figure 4a. Furthermore, the calculated ECSA and  $Q_{Pt-Red}$  charge are given in Figure 4b.

The cycling in  $N_2$  and resulting CV curves show minor changes in the double layer region ( $0.35$ – $0.55 V_{RHE}$ ) and faradaic currents at Pt oxidation ( $0.80$ – $1.00 V_{RHE}$ ) and Pt oxide reduction region ( $0.40$ – $0.95 V_{RHE}$ ) as well as the decreasing of the onset over  $1.00 V_{RHE}$  within cycling occurs. These minor changes are reflected in the ECSA and  $Q_{Pt-Red}$  charge (Figure 4b). While the developments for the trimetallic PtNiMo/C catalyst are significant, the ECSA and  $Q_{Pt-Red}$  for single Pt/C show nearly constant values. The ECSA values varies between  $80$  to  $89 m^2 g_{Pt}^{-1}$  (approximately 10%), which result in half of the deviation compared to the PtNiMo/C catalyst. Moreover, the  $Q_{Pt-Red}$  charge varies between  $2378$  to  $2531 \mu C cm_{Pt}^{-2}$  resulting in higher values in compare to  $1200 \mu C cm_{Pt}^{-2}$  after 23 cycles for PtNiMo/C and minor deviation of approximately 6% ( $> 50%$  for PtNiMo/C).

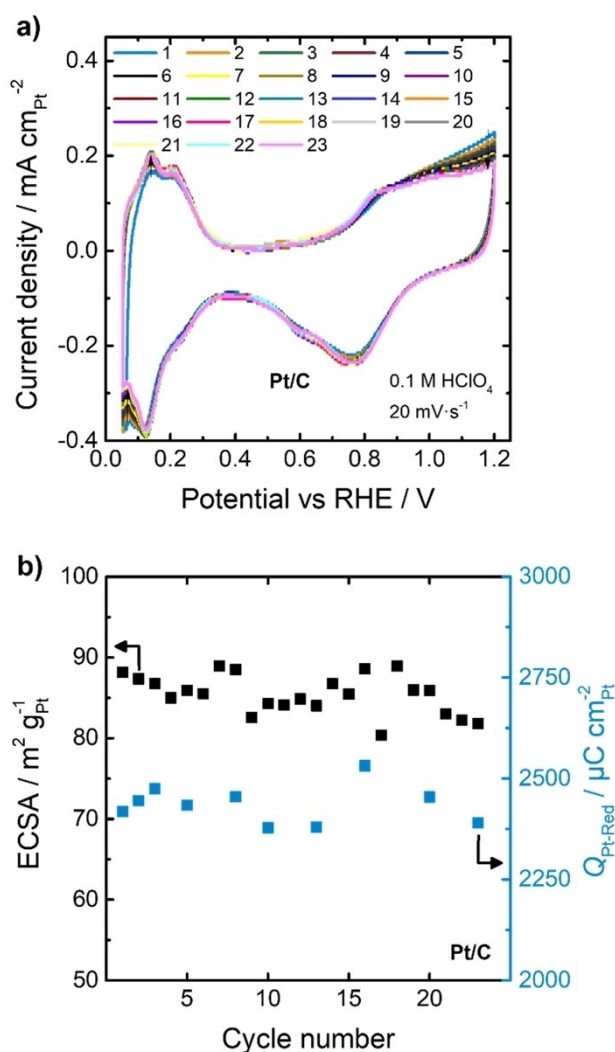


**Figure 4.** a) CV development of single Pt/C catalyst with pretreatment. b) Calculated ECSA and  $Q_{Pt-Red}$  charge with increasing cycle number. Recorded in  $N_2$ -saturated  $0.1 M HClO_4$  electrolyte in potential range of  $0.05$ – $1.20 V_{RHE}$  and scan-rate of  $20 mV s^{-1}$ .

Within these results we can make the assumption, that the stronger CV development and change of ECSA and  $Q_{\text{Pt-Red}}$  for the PtNiMo/C is associated to the leaching behavior of the transition metals (Ni, Mo) and exposition of Pt active sites during cycling. On the other hand, the single Pt/C seems to have minor changes and overall constant values. It needs to be noted that it cannot be ruled out that an unknown pretreatment during the production of the commercial Pt/C could also be reason for the different initial behavior.

### Combining cycling in $\text{N}_2$ and $\text{O}_2$ saturated electrolyte to study the highly active regime

While the previous studies have allowed to follow changes during the cycling to be tracked in either  $\text{N}_2$  or  $\text{O}_2$  saturated electrolyte, it is unclear how to combine the findings obtained, e.g. on cathodic reductive current of oxidized Pt and activity at a specific cycle.

To clarify this question, three different types of experiments were carried out and are given as scheme (Scheme S1 in the Supporting Information):

- i) Starting with cycling in  $\text{O}_2$  saturated electrolyte to varying cycle numbers (LSV) and then saturating with  $\text{N}_2$  for obtaining a single CV at this specific cycle number;
- ii) Starting with cycling in  $\text{N}_2$  saturated electrolyte to varying cycle numbers (CV) and then saturating with  $\text{O}_2$  for determining activity at this specific cycle number (LSV);
- iii) Alternating  $\text{N}_2$  and  $\text{O}_2$  saturation between every cycle.

Figure S4 summarizes the results of the experiments of type i and ii. For comparison, the open symbols in Figure S4 represent the average activity results from solely cycling in  $\text{O}_2$  saturated electrolyte (Figure 3c) and the filled symbols are from an individual new experiment with ORR polarization curves (squares) or CVs in  $\text{N}_2$  saturated electrolyte (triangles) up to this cycle number. Similar to the prior observation during repeating the experiment, the absolute number of activities differs and as every data point represents a new electrode and experiment, the deviations are rather large (e.g. 15–18% at 6<sup>th</sup> cycle). Nevertheless, the general trend remains similar between cycling in  $\text{N}_2$  and  $\text{O}_2$  saturated electrolyte. A fast increase of activity within the first five to eight cycles takes place followed by a slower decrease. A closer look into the individual development of selected activities up to the point (Figure S5a) or after the point of changing the gas atmosphere (Figure S5b) corroborates the trend even further.

Figure 5 presents the development of Pt reduction charge ( $Q_{\text{Pt-Red}}$ ) resulting after a specific number of ORR cycles (type i experiment) or specific number of cycles in  $\text{N}_2$  atmosphere (type ii experiment). An increase of the charge from the first to the 23<sup>rd</sup> cycle is observed for both types of experiments and is similar to the prior observed one (unfilled squares, Figure 2b), but also differences get obvious. Cycling in  $\text{N}_2$  saturated electrolyte starts with less Pt oxidation and thus lower reduction charge of  $1170 \mu\text{C cm}_{\text{Pt}}^{-2}$  at 6<sup>th</sup> cycle compare to  $1390 \mu\text{C cm}_{\text{Pt}}^{-2}$  for the  $\text{O}_2$  saturated electrolyte. Nevertheless, a

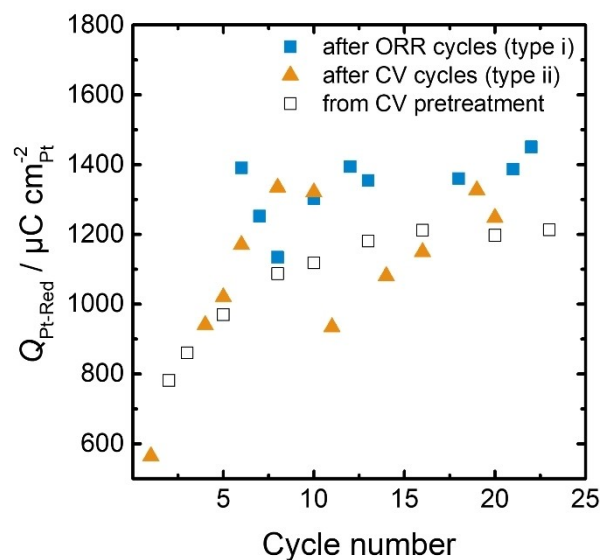


**Figure 5.** Charge of Pt reduction ( $Q_{\text{Pt-Red}}$ ) from CVs in  $\text{N}_2$  saturated 0.1 M  $\text{HClO}_4$  solution after ORR cycles (blue squares, type i), after CV cycles (orange triangles, type ii) and from prior CV pretreatment experiment (unfilled squares) (Figure 2b).

similar high charge of 1330 to  $1450 \mu\text{C cm}_{\text{Pt}}^{-2}$  results after 23 cycles. The observed difference most likely stems from the higher reactivity of dissolved molecular oxygen compared to water as oxidizing agent. However, from the CVs obtained (Figure S6), no correlation how the ECSA develops during these different pretreatment cycles can be obtained. The scattering from preparing a new electrode for every data point seems to overlay the changes observed in Figure 2 for a single electrode.

In order to reduce the scattering from preparation of new experiments at every data point and to see a clear trend, the experiment of type iii is very helpful (Figure 6). The development of the SA and MSA at  $0.95 V_{\text{RHE}}$  shows a clear trend, with an initial SA of  $0.24 \text{ mA cm}_{\text{Pt}}^{-2}$ , a sharp increase to the maximum at the 5<sup>th</sup> cycle and a slower subsequent drop of activity. The ECSA and Pt reduction charge ( $Q_{\text{Pt-Red}}$ ) show similar developments and achieve nearly the exact values as the experiment in CV pretreatment with one electrode (Figure 2b). These results prove that the activity development mainly occur from the intrinsic changes of nanoparticles and active sites by adsorption/desorption mechanism as the electrolyte was not changed and re-deposition of previous leached metals can take place.<sup>[39,40]</sup>

The sum of experiments allows to deduce a very similar picture for pretreatment in  $\text{N}_2$  or  $\text{O}_2$  saturated electrolyte. The slightly different oxidation power from  $\text{N}_2$  or  $\text{O}_2$  saturated electrolyte might lead to minor differences, e.g. in position of the maximum activity.

For direct comparison the type iii experiment was carried out for the Pt/C catalyst and results are shown in Figure 7. The SA and MSA values at  $0.95 V_{\text{RHE}}$  (Figure 7a) remain nearly constant between  $0.045$  to  $0.055 \text{ mA cm}_{\text{Pt}}^{-2}$ , at lower values and without the initial increase compared to PtNiMo/C. The ECSA and  $Q_{\text{Pt-Red}}$  in Figure 7b also results in minor changes

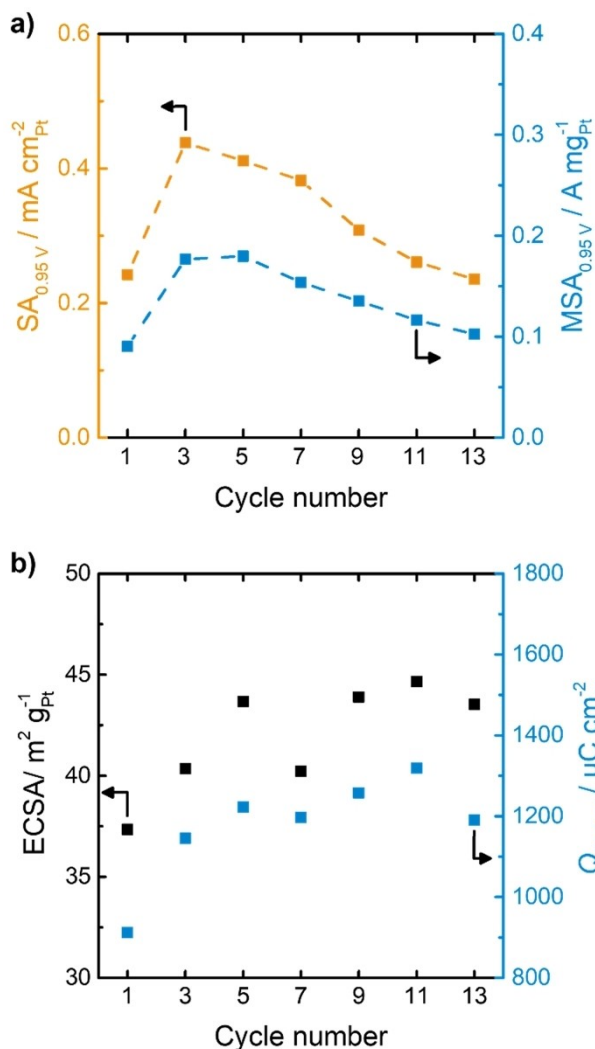


**Figure 6.** a) Activity development by alternating atmosphere between  $\text{N}_2/\text{O}_2$  in the same electrolyte after each activity point at  $0.95 V_{\text{RHE}}$ . b) Development of ECSA and  $Q_{\text{Pt-Red}}$  at specific cycle number. Potential range:  $0.05\text{--}1.20 V_{\text{RHE}}$  at  $20 \text{ mV s}^{-1}$ , ORR with rotation at  $1600 \text{ rpm}$  in  $0.1 \text{ M HClO}_4$ .

between  $72\text{--}80 \text{ m}^2 \text{g}_{\text{Pt}}^{-1}$  in ECSA and  $1663\text{--}1890 \mu\text{C cm}_{\text{Pt}}^{-2}$  in  $Q_{\text{Pt-Red}}$ , respectively. The overall activity development in Pt/C in alternating  $\text{N}_2/\text{O}_2$  cycles in the same electrolyte, as well as the minor changes in Figure 4 with CV cycle pretreatment confirming the unchanged surface of Pt/C, resulting in stable activity values with increasing cycle numbers. In addition, this type iii experiment confirms the dependence of the SA, MSA, ECSA and  $Q_{\text{Pt-Red}}$  changes from the leaching behavior of the transition metals at the PtNiMo/C catalyst.

### Identifying dynamics of the catalyst surface during cycling

To identify changes in the adsorption sites, we probed the surface with CO and performed stripping experiments by CV and electrochemical infrared reflection absorption spectroscopy (EC-IRRAS) in successive cycles. Specifically, one cycle consists of the following steps: (i) adsorption of CO from

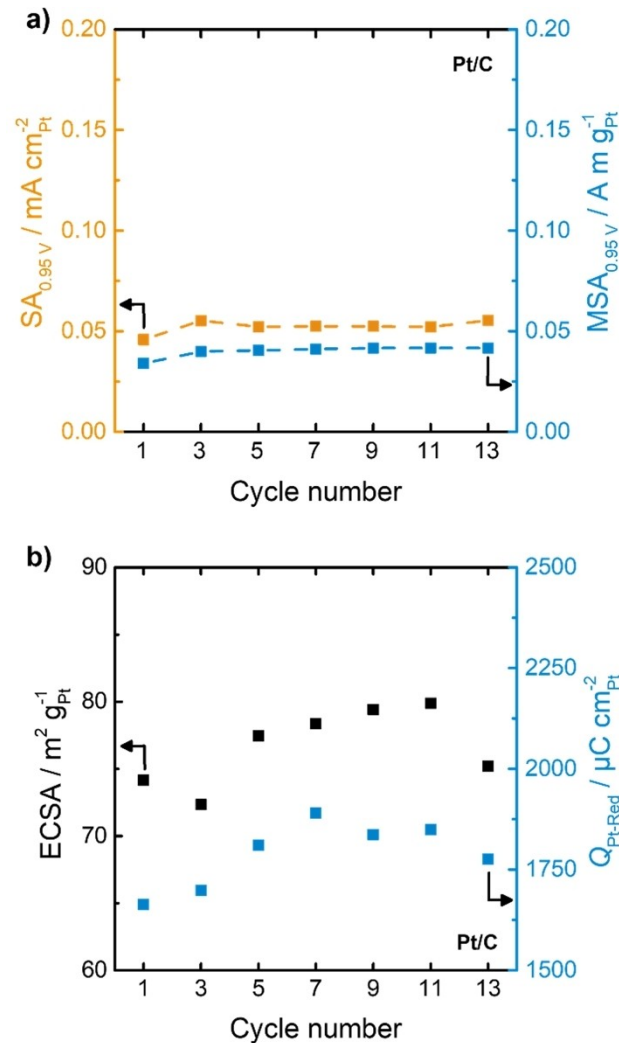


**Figure 7.** Comparison measurements with single Pt/C catalyst. a) Activity development by alternating atmosphere between  $\text{N}_2/\text{O}_2$  in the same electrolyte after each activity point at  $0.95 V_{\text{RHE}}$ . b) Development of ECSA and  $Q_{\text{Pt-Red}}$  at specific cycle number. Potential range:  $0.05\text{--}1.20 V_{\text{RHE}}$  at  $20 \text{ mV s}^{-1}$ , ORR with rotation at  $1600 \text{ rpm}$  in  $0.1 \text{ M HClO}_4$ .

solution, (ii) removal of CO from solution by purging with argon, and (iii) the measurements themselves by CV or EC-IRRAS in a potential window between  $0.05$  and  $1.2 V_{\text{RHE}}$  (see Figure 8a). In CV (Figure 8b), we observe in the first cycle a pre-peak at  $0.45 V_{\text{RHE}}$  (light green), a main feature at  $0.75 V_{\text{RHE}}$  (dark green), and an additional feature at  $0.82 V_{\text{RHE}}$ . In the subsequent cycles, the pre-peak at  $0.45 V_{\text{RHE}}$  decreases strongly, the main feature remains, becomes sharper and shifts slightly to  $0.73 V_{\text{RHE}}$ . The peak at  $0.82 V_{\text{RHE}}$  disappears completely. For more than five cycles, an additional feature appears at  $0.80 V_{\text{RHE}}$  (pink), which increases in intensity as the number of cycles increases. Within the first 10 cycles, we observe an increase in the integrated peak area by a factor of 1.2, which levels off afterwards (see Supporting Information Figure S8). Note that the integrated peak area is proportional to the number of adsorption sites. The feature at  $0.73 V_{\text{RHE}}$  is attributed to CO adsorption on Pt facet sites. The feature at

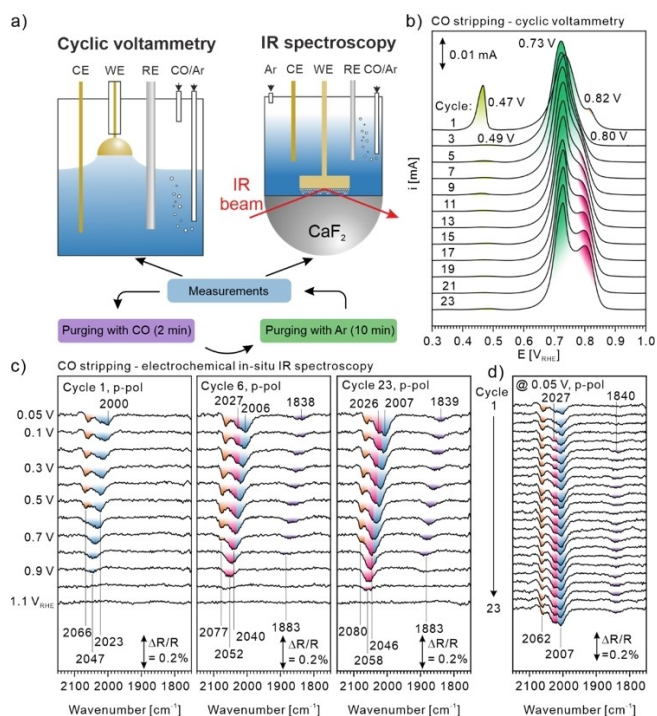


**Figure 8.** CO stripping experiment on PtNiMo–C catalyst with CV and EC-IRRAS in 23 cycles; a) experimental procedure, b) cyclic voltammograms, c) potential dependent IR spectra, and d) cycle dependent IR spectra measured at 0.05 V<sub>RHE</sub>. All measurements were performed in 0.1 M HClO<sub>4</sub>. In the CVs always the subsequent cycle without CO adsorbed was used as a background. IR spectra are referenced to a spectrum at 1.2 V recorded after CO stripping and we corrected the baseline.

0.45 V<sub>RHE</sub> is in perfect agreement with CO adsorbed on Pt sites near NiO<sub>xr</sub><sup>[41]</sup> and the initial peak at 0.82 V<sub>RHE</sub> we assign to CO adsorption on Pt in PtMo.<sup>[42]</sup> The strong decrease of both signals in the subsequent cycle indicates that after the first cycle Ni and Mo are dissolved largely from the surface and remain in the subsurface only. To identify the feature at 0.80 V<sub>RHE</sub> appearing in consecutive cycles, we followed the oxidation by EC-IRRAS. In Figure 8c we show the potential dependent IR spectra of the CO oxidation at 3 representative cycle numbers, namely cycle 1, 6, and 23. A comparison of the spectra measured at 0.05 V<sub>RHE</sub> for all 23 cycles is shown in Figure 8d. Note that all spectra are referenced to a CO free spectrum measured at 1.2 V<sub>RHE</sub> after oxidation. In the first cycle at 0.05 V<sub>RHE</sub>, we identify two distinct bands, a sharp band at 2062 cm<sup>-1</sup> (orange) and broader band at 2000 cm<sup>-1</sup> (blue). With increasing potential, the bands at 2062 and 2000 cm<sup>-1</sup> disappear at 0.7 and 1.0 V<sub>RHE</sub>, respectively. The stretching frequency of the band at 2062 cm<sup>-1</sup> is in perfect agreement with CO adsorption in the on top position (CO<sub>t</sub>) on Pt facet sites.<sup>[43,44]</sup> A redshift of the CO band occurs for CO<sub>t</sub> adsorption on low coordinated adsorption sites<sup>[45]</sup> as well as for Pt atoms neighboring Ni atoms (both in the surface layer as well as in the subsurface layer).<sup>[43]</sup> As we expect such sites to be present in the initial PtNiMo alloy, we assign the band at 2000 cm<sup>-1</sup> mainly to Pt atoms neighboring the alloying metals. Note that we do not exclude additional contributions

from low coordinated adsorption sites as well. As the number of cycles increases, two additional features appear. An additional band is observed at 1840 cm<sup>-1</sup> (purple), which we attribute to bridge bonded CO (CO<sub>b</sub>). This feature is indicative of larger Pt facets.<sup>[44]</sup> Second, we observe an additional band at 2027 cm<sup>-1</sup> (pink), which increases in intensity with increasing cycle number. The latter feature becomes the dominant band at potentials above 0.7 V<sub>RHE</sub>. We conclude that this feature is responsible for the peak in the CV at 0.8 V<sub>RHE</sub> that develops with increasing cycle number. We attribute this feature to the formation of small Pt clusters.<sup>[45]</sup> In general, we could observe an increase in available surface Pt sites, due to dissolution of surface Mo and Ni, formation of larger facets, and formation of small Pt clusters approx. during the first 10 cycles, which agree very well with the observed increase in Q<sub>Pt-Red</sub> and the strong increase in activity during these initial cycles. While the higher activity of Pt facets is known and could be major reason for activity increase, an additional activity stemming from the very small Pt clusters, probably also single atoms, can also not be ruled out.

As the dissolution of the PtNiMo surface is essential for the observed dynamics of the catalyst surface and strong activity changes during the first cycles electrochemical online scanning flow cell ICP-MS measurements (SFC-ICP-MS) were carried out to get further insights into the dissolution behavior during the first cycles (see Supporting Information Figure S10). The SFC-ICP-MS results show some minor dissolution of the Pt, not too far from detection limit. As reported in literature the addition of Mo suppresses the dissolution of Nickel<sup>[20]</sup> and no distinct dissolution peaks can be observed during cycling, and the initial dissolution while holding for 300 s at 0.05 V<sub>RHE</sub> is the only significant contribution to Ni-dissolution-currents. Molybdenum behaves very similar as Nickel. Thus, only very small dissolution events close or below to the detection limit lead to the restructuring observed by CO stripping and EC-IRRAS. The observed Pt dissolution is very likely the source for formation of small Pt clusters.

### Influence of electrolyte exchange on the activity

Interestingly, CO stripping an EC-IRRAS gave no explanation for the observed decrease in activity after 10 to 15 cycles. As it is known from accelerated stress tests that impurities accumulating in the electrolyte during cycling can lead to underestimation of catalyst activity, the experiment iii) of section 3.3. was carried out with exchanging the electrolyte to a fresh one after every single polarization curve (Figure 9a). The activity course results in an elongated shape in comparison to the measurement without electrolyte exchange (Figure 9b) and shows a lower decrease in SA after the maximum. In total, the electrolyte refreshing allows to resolve the activity without overlaying electrolyte dependent deactivation. As a result, the maximum in the activation process shifts to the 11<sup>th</sup> cycle with a SA of 3.00 mA cm<sub>Pt</sub><sup>-2</sup> and MSA of 1.37 A mg<sub>Pt</sub><sup>-1</sup> (both at 0.90 V<sub>RHE</sub>), respectively. In

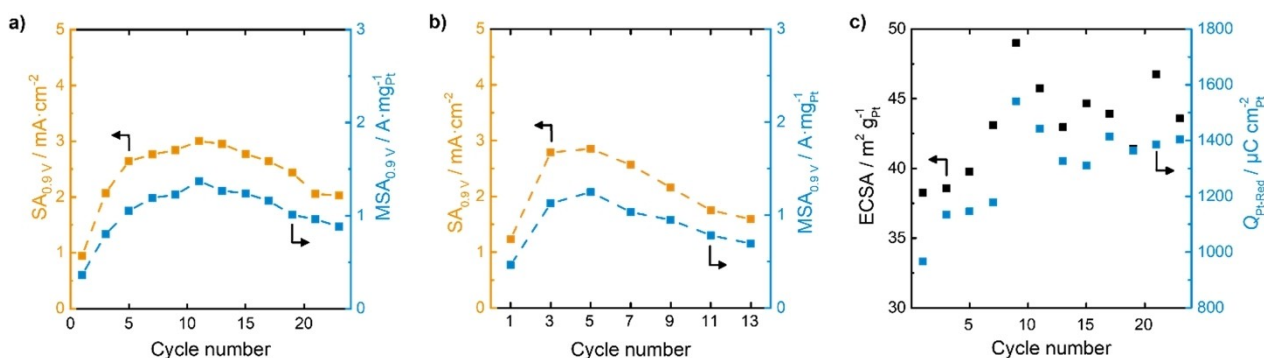


**Figure 9.** Influence of electrolyte refreshing to activity. a) Electrolyte refreshing after each cycle in alternating  $\text{N}_2/\text{O}_2$  atmosphere at  $0.9\text{ V}_{\text{RHE}}$ . b) Alternating  $\text{N}_2/\text{O}_2$  atmosphere in the same electrolyte after each cycle at  $0.9\text{ V}_{\text{RHE}}$ . c) ECSA values and  $Q_{\text{Pt-Red}}$  calculated for each cycle number. Potential range:  $0.05\text{--}1.20\text{ V}_{\text{RHE}}$ . SA recorded at  $20\text{ mVs}^{-1}$  and  $1600\text{ rpm}$  rotation in  $\text{O}_2$ -saturated  $0.1\text{ M HClO}_4$ .

addition, in Figure 9c, the ECSA after each activity point show the known behavior, which results in an increase till the 11<sup>th</sup> cycle starting from  $38\text{ m}^2\text{g}_{\text{Pt}}^{-1}$  and resulting in  $42$  to  $48\text{ m}^2\text{g}_{\text{Pt}}^{-1}$ . Further, the calculated  $Q_{\text{Pt-Red}}$  present a continuing increase with fluctuation along the cycle number and a decrease in the value after the 19<sup>th</sup> cycle. One reason for higher fluctuation may stem from the change in the activation method. As cycling in  $\text{N}_2$  takes place without any rotation, the RDE rotation of  $1600\text{ rpm}$  are chosen for ORR in  $\text{O}_2$ . During leaching, adsorption/desorption and contamination processes are the main reason for the catalyst changing and can be influenced through the accelerated mass transfer provided by the rotation. Additional electrolyte exchange removes impurities at the surface of the catalyst and electrolyte, while adsorbed species (e.g.  $\text{OH}^*/\text{O}^*$ ) remain.<sup>[46,2]</sup> With this knowledge one can make the assumption that in the chosen potential range of  $0.05\text{--}1.20\text{ V}_{\text{RHE}}$  leached available impurities, e.g.  $\text{Cl}^-$ -ions or organics from catalyst preparation (reducing agent), have the possibility to re-deposit on the catalyst surface and show an influence to the faster activation process in comparison to the refreshing method. Moreover, the electrolyte refreshing has a noticeable influence to the SA even after short cycle numbers and not only according to long conditioning methods, e.g. after accelerated durability test (ADT).

In total still a deactivation after approx. 10 cycles is observed. While the characterization methods applied show no changes of the catalyst surface, the very low but constant Pt dissolution is the only hint for a reason and further studies are necessary to understand thus deactivation.

## Conclusion

In conclusion, activity changes of PtNiMo/C during initial pretreatment were determined alongside with the electrochemical active surface area. During pretreatment, a steady CV profile does not correspond to a steady activity and a closer look into the activity is necessary. A pronounced activity increase could be observed during the first five to eight cycles

and maximum activities of  $0.57\text{ mA}\cdot\text{cm}_{\text{Pt}}^{-2}$  at  $0.95\text{ V}_{\text{RHE}}$  were observed. The observed trend in activity remains similar when carrying out cyclic voltammograms in  $\text{N}_2$  and  $\text{O}_2$  saturated electrolyte. While the activity increased by a factor of 2.3, the ECSA increased only by a factor of 1.2. The activity increase can be correlated to a restructuring of the surface with very low dissolution observable. Thereby larger Pt facets are created, surface features of Pt-alloy components are vanishing, and small size Pt clusters are forming.

Interestingly, despite the very low number of ORR polarization curves taken, electrolyte refreshing has for the alloy catalysts a strong influence and needs to be carried out to avoid electrolyte-based deactivation. While the phenomenon is known, it is normally only accounted for during accelerated stress tests with orders of magnitude higher cycle numbers. Interestingly, CO stripping and electrochemical infrared reflection absorption spectroscopy provide important insights why the activity increase is observed during the first cycles, but no explanation for the observed decrease afterwards. Further studies are needed to understand this deactivation behavior in more detail. In general studying the pretreatment phase of alloy catalysts is highly attractive and gives access to information on highly active species. Furthermore, classical RDE protocols developed for monometallic catalysts need probably to be adapted and steady CV during pretreatment is not a sufficient indicator for finished pretreatment. Future method development needs to follow on this aspect.

## Experimental Section

### Materials

$\text{Pt}(\text{acac})_2$  (98%) and  $\text{Mo}(\text{CO})_6$  (98%) were purchased from Acros Organics.  $\text{Ni}(\text{acac})_2$  (95%) was purchased from Sigma-Aldrich. Perchloric acid (70%) was purchased from Carl Roth or Sigma Aldrich (99.999% trace metals basis). *N,N*-Dimethylformamide (99.8 + %) and HiSpec-3000 (20 wt.-% Pt on carbon black; named Pt/C within the manuscript) were purchased from Alfa Aesar. Benzoic acid (99%) was purchased from Merck Millipore. Deionized water



(<1.0  $\mu\text{S cm}^{-1}$ ) from VWR chemicals or ultrapure water (MilliQ synergy UV, 18.2 M $\Omega\text{cm}$  at 25 $^\circ$ , <5 ppb TOC) was used for preparation of all aqueous solutions. All chemicals were used as received without further purification.

### Synthesis of PtNiMo/C catalyst

The synthesis of carbon supported octahedral shaped PtNiMo catalyst was performed by using a surfactant free solvothermal method following literature procedures.<sup>[29,35]</sup> Detailed information can be found in the Supporting Information.

### Instrumentation

The determination of the exact loadings of Pt, Ni and Mo on the catalyst samples were done using inductively coupled plasma optical emission spectroscopy (ICP-OES, Optima 2000DV, PerkinElmer). The powder X-ray diffraction (XRD) patterns are measured on a StadiP (Stoe) using a Ge(111) monochromator with Cu K $\alpha$  radiation ( $\lambda = 1.54060 \text{ \AA}$ ). STEM images were recorded using a JEM2100F (JEOL) with a field emission gun operating at a nominal acceleration voltage of 200 kV. The structural characterizations are given in Figure S1 in the Supporting Information. Samples for transmission electron microscopy (TEM) were prepared by dip-coating TEM grids with suspensions of catalyst powder in isopropanol and water, followed by drying in the air and plasma cleaning for 1 min utilizing a Tergeo EM plasma cleaner (PIE Scientific). Conventional and high-resolution TEM, high-angle annular dark field (HAADF) scanning TEM (STEM), and spectrum images using EDXS were acquired using a Talos F200i (Thermo Fisher Scientific, former FEI). The microscope, equipped with a Schottky emitter and two Bruker XFlash 6T-100 EDS detectors, was operated at an acceleration voltage of 200 kV.

### Electrochemical Measurements

The electrochemical measurements were carried out on an OctoStat200 multichannel potentiostat (IVIUM Technologies), which is controlled by IviumSoft. As counter electrode, a graphite rod (PINE) and a leak-free double-junction 3 M KCl Ag/AgCl electrode (Aldrich) as reference electrode was used, respectively. All potentials reported here were calibrated against the reversible hydrogen electrode (RHE), if not declared otherwise. A glassy-carbon rotating disk electrode (GC-RDE, 5 mm diameter, PINE) was used as the working electrode. Prior to each experiment, the RDE was polished on a pad with 0.3  $\mu\text{m}$  alumina polishing solution and cleaned ultrasonically with acetone, ethanol and deionized water to remove contaminations. A catalyst ink in total of 2 mL was prepared by sonicating a suspension of catalyst powder in a mixture of 3:1 ethanol:deionized water and 5% Nafion for PtNiMo/C catalyst and a mixture of 3:1 deionized water:ethanol and 5% Nafion for Pt/C catalyst. The ionomer/carbon ratio was set at 0.55  $\text{gg}^{-1}$  for all measurements. Furthermore, a calibrated amount of catalyst ink for a 2  $\mu\text{g}$  Pt loading (10  $\mu\text{g}_{\text{Pt}} \text{cm}^{-2}$ ) based on the RDE geometric area was applied onto the RDE and dried under argon flow. All electrochemical measurements were performed at room temperature in  $\text{N}_2$  or  $\text{O}_2$  saturated 0.1 M  $\text{HClO}_4$  solution and in the potential range of 0.05–1.20  $V_{\text{RHE}}$ . The ECSA value was determined by measuring the H adsorption charge from the CV curves at 20  $\text{mV s}^{-1}$ . For calibration, 210  $\mu\text{C cm}_{\text{Pt}}^{-2}$  were used as charge density for polycrystalline Pt.<sup>[2]</sup> Furthermore, the charge of Pt oxide reduction ( $Q_{\text{Pt-Red}}$ ) was calculated by identifying the Pt reduction peak in the area between the vertex of the cathodic current and non-faradaic currents at 0.40  $V_{\text{RHE}}$ . ORR measurements were carried out recording polarization curves in  $\text{O}_2$  saturated 0.1 M  $\text{HClO}_4$

solution at 20  $\text{mV s}^{-1}$  and a rotation of 1600 rpm. As reliable kinetic information can only be obtained at current densities well below diffusion limiting current densities, specific activities are reported at 0.95  $V_{\text{RHE}}$ . Additionally, activities at 0.9  $V_{\text{RHE}}$  are given in the SI, to allow comparison to other literature data. Prior to each ORR activity measurement, the electrolyte was purged for a minimum of 20 min with high purity oxygen and an  $\text{O}_2$  flow was maintained to avoid any disturbance from ambient atmosphere during the measurements. Further information on the electrochemical measurements are summarized in the Supporting Information.

CO stripping was carried out measuring cyclic voltammetry in 0.1 M  $\text{HClO}_4$  with a three-electrode setup in a home-built cell. The measurements were performed in the so-called hanging meniscus configuration. We deposited catalyst ink on a bead-type gold electrode. A gold wire was used as the counter electrode (CE) and a reversible hydrogen electrode (RHE) as the reference electrode (RE). We used a commercial potentiostat (Gamry, Reference [600]) and controlled the potential throughout the measurement. CO (Linde 4.7) was adsorbed at 0.05  $V_{\text{RHE}}$  for 2 min and then the solution was purged with Ar for 10 min. We then recorded two cyclic voltammograms between 0.05 and 1.2  $V_{\text{RHE}}$  at a scan rate of 20  $\text{mV} \cdot \text{s}^{-1}$ . We calculated the peak area using the second cycle as a baseline. The procedure was repeated 12 times. To measure electrochemical infrared reflection absorption spectroscopy (EC-IRRAS) we used a commercial IR spectrometers with evacuated optics (Bruker Vertex 80v) and a liquid nitrogen cooled mercury cadmium telluride (MCT) narrow band detector. The spectrometer was equipped with a commercial optics for electrochemical measurements, a home-built electrochemical cell and a polarizer. We used a  $\text{CaF}_2$  hemisphere (Korth) as IR transparent window material sealed with a Kalrez gasket. We controlled the potential with a commercial potentiostat (Gamry Reference [600]). We deposited the catalyst ink on a gold substrate with a surface area of 1.1  $\text{cm}^2$ . We used an Au wire as the counter electrode and a home build RHE as reference electrode. Spectra were measured with p-polarized light. CO (Linde 4.7) was adsorbed at 0.05  $V_{\text{RHE}}$  for 2 min. Subsequently we purged the solution with Ar for 10 min. We increased then stepwise the potential from 0.05 V to 1.2  $V_{\text{RHE}}$  in 0.1 V steps. At each step, we acquire IR spectra with 128 scans per spectrum, a resolution of 2  $\text{cm}^{-1}$ , and an acquisition time of 57 s. We subsequently decreased the potential back to 0.05  $V_{\text{RHE}}$  with a scan rate of 20  $\text{mV} \cdot \text{s}^{-1}$ . This procedure was repeated 23 times. For a more detailed description of the IR setup used, we refer to literature.<sup>[47]</sup>

Electrochemical online scanning flow cell ICP-MS measurements (SFC-ICP-MS) were conducted using a three-electrode setup with a Gamry Reference [620]. A glassy carbon rod was used as counter electrode and a HydroFlex RHE (gaskatel) as reference electrode. The ink was prepared, suspending the catalyst powder in a 3:1 mixture of ethanol and water and 5% Nafion solution, with an I/C ratio of 0.55. The ink concentration was adjusted so that a loading of approx. 1.5  $\mu\text{g}_{\text{Pt}} \text{cm}^{-2}$  was obtained. After ultrasonication with an ultrasonic horn, the ink was drop-cast on a polished GC plate. All SFC-ICP-MS measurements were performed in Ar saturated 0.1 M  $\text{HClO}_4$  electrolyte. For ICP-MS (Agilent 7900, Agilent Technologies) measurements Pt149, Ni58, and Mo92 were used as analytes, Co59 and Re187 as internal standards. Dissolution rates were measured at an experimentally determined analyte flow rate of approx. 5.8  $\mu\text{s}^{-1}$ . To detect the elemental dissolution of catalyst contents, the potential of the working electrode was held at 0.05  $V_{\text{RHE}}$  for 300 s initially. Then 20 CVs between 0.05 and 1.2  $V_{\text{RHE}}$  were performed at a cycling rate of 20  $\text{mV s}^{-1}$ , before holding 0.05  $V_{\text{RHE}}$  for 300 s again.

## Supporting Information

Additional references cited within the Supporting Information.<sup>[23,29,35,48]</sup>

## Acknowledgements

The authors acknowledge Nicolai Schmitt for help on electrochemical experiments during the revision and Dominik Dworschak for scientific discussion on SFC-ICP-MS experiments. B.E. acknowledges the funding from the European Research Council (ERC) under the European Union's Horizon 2020 research and innovation program (grant agreement No. 681719). J.L. and K.M. acknowledge financial support by the Deutsche Forschungsgemeinschaft (DFG) via Collaborative Research Centre SFB 1452 – Catalysis at Liquid Interfaces (project 431791331). OB acknowledges financial support by the DFG (project 431733372). M.L. acknowledges the Federal Ministry of Education and Research (BMBF) in the framework of NanoMatFutur (SynKat, FK: 03XP0265) for financial support. K.J.J.M. and P.L.D. acknowledge the financial support by the Federal Ministry of Education and Research (BMBF) of Germany in the programme H2GIGA-HyThroughGen (Project Identification Number: 03HY108A). J.Y. acknowledges the support provided by the China Scholarship Council (CSC). G.-R.Z. acknowledges the funding from the National Natural Science Foundation of China (NSFC, No. 22272117) and Shanghai Cooperation Organization Science and Technology Partnership Project (No. 2021E01009). Open Access funding enabled and organized by Projekt DEAL.

## Conflict of Interests

The authors declare no conflict of interest.

## Data Availability Statement

The data that support the findings of this study are available from the corresponding author upon reasonable request.

**Keywords:** Alloyed Catalyst · Cyclic voltammetry · Electrochemistry · Oxygen Reduction · Pretreatment · Rotating Disk Electrode

- [1] L. Huang, S. Zaman, X. Tian, Z. Wang, W. Fang, B. Y. Xia, *Acc. Chem. Res.* **2021**, *54*, 311–322.
- [2] H. A. Gasteiger, S. S. Kocha, B. Sompalli, F. T. Wagner, *Appl. Catal. B* **2005**, *56*, 9–35.
- [3] J. C. Meier, C. Galeano, I. Katsounaros, J. Witte, H. J. Bongard, A. A. Topalov, C. Baldizzone, S. Mezzavilla, F. Schüth, K. J. J. Mayrhofer, *Beilstein J. Nanotechnol.* **2014**, *5*, 44–67.
- [4] E. Pizzutilo, S. Geiger, J. P. Grote, A. Mingers, K. J. J. Mayrhofer, M. Arenz, S. Cherevko, *J. Electrochem. Soc.* **2016**, *163*, F1510–F1514.
- [5] A. S. B. Federico Calle-Vallejo, J. Tymoczko, V. Colic, Q. Huy Vu, M. D. Pohl, K. Morgenstern, D. Loffreda, P. Sautet, W. Schuhmann, *Science* **2015**, *350*, 185–190.

- [6] P. Strasser, S. Koh, T. Anniyev, J. Greeley, K. More, C. Yu, Z. Liu, S. Kaya, D. Nordlund, H. Ogasawara, *Nat. Chem.* **2010**, *2*, 454.
- [7] V. R. Stamenkovic, B. Fowler, B. S. Mun, G. Wang, P. N. Ross, C. A. Lucas, N. M. Marković, *Science* **2007**, *315*, 493–497.
- [8] P. Strasser, M. Gliech, S. Kuehl, T. Moeller, *Chem. Soc. Rev.* **2018**, *47*, 715–735.
- [9] C. Chen, Y. Kang, Z. Huo, Z. Zhu, W. Huang, H. L. Xin, J. D. Snyder, D. Li, J. A. Herron, M. Mavrikakis, M. Chi, K. L. More, Y. Li, N. M. Markovic, G. A. Somorjai, P. Ayng, V. R. Stamenkovic, *Science* **2014**, *343*, 1339–1343.
- [10] S. Polani, K. E. MacArthur, M. Kligenhof, X. Wang, P. Paciok, L. Pan, Q. Feng, A. Kormányos, S. Cherevko, M. Heggen, P. Strasser, *ACS Catal.* **2021**, *11*, 11407–11415.
- [11] C. Cui, L. Gan, M. Heggen, S. Rudi, P. Strasser, *Nat. Mater.* **2013**, *12*, 765–771.
- [12] C. Cui, M. Ahmadi, F. Behafarid, L. Gan, M. Neumann, M. Heggen, B. R. Cuenya, P. Strasser, *Faraday Discuss.* **2013**, *162*, 91–112.
- [13] V. R. Stamenkovic, B. S. Mun, M. Arenz, K. J. J. Mayrhofer, C. A. Lucas, G. Wang, P. N. Ross, N. M. Markovic, *Nat. Mater.* **2007**, *6*, 241–247.
- [14] V. R. Stamenkovic, B. S. Mun, K. J. J. Mayrhofer, P. N. Ross, N. M. Markovic, *J. Am. Chem. Soc.* **2006**, *128*, 8813–8819.
- [15] S. Kühn, M. Gocyla, H. Heyen, S. Selve, M. Heggen, R. E. Dunin-Borkowski, P. Strasser, *J. Mater. Chem. A* **2019**, *7*, 1149–1159.
- [16] R. Chattot, I. Martens, M. Scohy, J. Herranz, J. Drnec, F. Maillard, L. Dubau, *ACS Energy Lett.* **2020**, *5*, 162–169.
- [17] F. Dionigi, C. C. Weber, M. Primbs, M. Gocyla, A. M. Bonastre, C. Spöri, H. Schmies, E. Hornberger, S. Kühn, J. Drnec, *Nano Lett.* **2019**, *19*, 6876–6885.
- [18] P. J. Ferreira, G. J. la O', Y. Shao-Horn, D. Morgan, R. Makharia, S. Kocha, H. A. Gasteiger, *J. Electrochem. Soc.* **2005**, *152*, A2256.
- [19] J. Knossalla, P. Paciok, D. Göhl, D. Jalalpoor, E. Pizzutilo, A. M. Mingers, M. Heggen, R. E. Dunin-Borkowski, K. J. J. Mayrhofer, F. Schüth, *J. Am. Chem. Soc.* **2018**, *140*, 15684–15689.
- [20] Q. Jia, Z. Zhao, L. Cao, J. Li, S. Ghoshal, V. Davies, E. Stavitski, K. Attenkofer, Z. Liu, M. Li, X. Duan, S. Mukerjee, T. Mueller, Y. Huang, *Nano Lett.* **2018**, *18*, 798–804.
- [21] R. M. Arán-Ais, F. Dionigi, T. Merzdorf, M. Gocyla, M. Heggen, R. E. Dunin-Borkowski, M. Gliech, J. Solla-Gullón, E. Herrero, J. M. Feliu, *Nano Lett.* **2015**, *15*, 7473–7480.
- [22] N. Erini, V. Beermann, M. Gocyla, M. Gliech, M. Heggen, R. E. Dunin-Borkowski, P. Strasser, *Angew. Chem. Int. Ed.* **2017**, *56*, 6533–6538.
- [23] M. George, G.-R. Zhang, N. Schmitt, K. Brunnengraber, D. J. S. Sandbeck, K. J. J. Mayrhofer, S. Cherevko, B. J. M. Etzold, *ACS Catal.* **2019**, *9*, 8682–8692.
- [24] V. Stamenkovic, B. S. Mun, K. J. J. Mayrhofer, P. N. Ross, N. M. Markovic, J. Rossmeisl, J. Greeley, J. K. Nørskov, *Angew. Chem.* **2006**, *118*, 2963–2967.
- [25] J. K. Nørskov, J. Rossmeisl, A. Logadottir, L. Lindqvist, J. R. Kitchin, T. Bligaard, H. Jonsson, *J. Phys. Chem. B* **2004**, *108*, 17886–17892.
- [26] K. J. J. Mayrhofer, D. Strmcnik, B. B. Blizanac, V. Stamenkovic, M. Arenz, N. M. Markovic, *Electrochim. Acta* **2008**, *53*, 3181–3188.
- [27] K. Shinozaki, J. W. Zack, R. M. Richards, B. S. Pivovar, S. S. Kocha, *J. Electrochem. Soc.* **2015**, *162*, F1144–F1158.
- [28] K. Shinozaki, J. W. Zack, S. Pylypenko, B. S. Pivovar, S. S. Kocha, *J. Electrochem. Soc.* **2015**, *162*, F1384–F1396.
- [29] X. Huang, Z. Zhao, L. Cao, Y. Chen, E. Zhu, Z. Lin, M. Li, A. Yan, A. Zettl, Y. M. Wang, *Science* **2015**, *348*, 1230–1234.
- [30] R. Wang, C. Xu, X. Bi, Y. Ding, *Energy Environ. Sci.* **2012**, *5*, 5281–5286.
- [31] B. A. Pinaud, A. Bonakdarpour, L. Daniel, J. Sharman, D. P. Wilkinson, *J. Electrochem. Soc.* **2017**, *164*, F321–F327.
- [32] A. Kneer, N. Wagner, C. Sadeler, A.-C. Scherzer, D. Gerteisen, *J. Electrochem. Soc.* **2018**, *165*, F805–F812.
- [33] C. A. Rice, P. Urchaga, A. O. Pistono, B. W. McFerrin, B. T. McComb, J. Hu, *J. Electrochem. Soc.* **2015**, *162*, F1175–F1180.
- [34] C. H. Cui, H. H. Li, X. J. Liu, M. R. Gao, S. H. Yu, *ACS Catal.* **2012**, *2*, 916–924.
- [35] M. K. Carpenter, T. E. Moylan, R. S. Kukreja, M. H. Atwan, M. M. Tessema, *J. Am. Chem. Soc.* **2012**, *134*, 8535–8542.
- [36] E. Padgett, V. Yarlagadda, M. E. Holtz, M. Ko, B. D. A. Levin, R. S. Kukreja, J. M. Ziegelbauer, R. N. Andrews, J. Ilavsky, A. Kongkanand, D. A. Muller, *J. Electrochem. Soc.* **2019**, *166*, F198–F207.
- [37] J. Snyder, I. McCue, K. Livi, J. Erlebacher, *J. Am. Chem. Soc.* **2012**, *134*, 8633–8645.
- [38] R. K. Ahluwalia, J.-K. Peng, X. Wang, D. A. Cullen, A. J. Steinbach, *J. Electrochem. Soc.* **2017**, *164*, F306–F320.

- [39] Y. Zhang, S. Chen, Y. Wang, W. Ding, R. Wu, L. Li, X. Qi, Z. Wei, *J. Power Sources* **2015**, *273*, 62–69.
- [40] M. Watanabe, H. Yano, H. Uchida, D. A. Tryk, *J. Electroanal. Chem.* **2018**, *819*, 359–364.
- [41] S. Rudi, C. Cui, L. Gan, P. Strasser, *Electrocatalysis* **2014**, *5*, 408–418.
- [42] L. C. Ordóñez, P. Roquero, P. J. Sebastian, J. Ramírez, *Int. J. Hydrogen Energy* **2007**, *32*, 3147–3153.
- [43] O. Brummel, F. Waidhas, I. Khalakhan, M. Vorokhta, M. Dubau, G. Kovács, H. A. Aleksandrov, K. M. Neyman, V. Matolín, J. Libuda, *Electrochim. Acta* **2017**, *251*, 427–441.
- [44] I. Villegas, M. J. Weaver, *J. Chem. Phys.* **1994**, *101*, 1648–1660.
- [45] O. Brummel, F. Waidhas, F. Faisal, R. Fiala, M. Vorokhta, I. Khalakhan, M. Dubau, A. Figueroba, G. Kovács, H. A. Aleksandrov, G. N. Vayssilov, S. M. Kozlov, K. M. Neyman, V. Matolín, J. Libuda, *J. Phys. Chem. C* **2016**, *120*, 19723–19736.
- [46] K. Schlögl, *Dissertation*, Technische Universität München, **2011**.
- [47] F. Faisal, M. Bertram, C. Stumm, F. Waidhas, O. Brummel, J. Libuda, *Rev. Sci. Instrum.* **2018**, *89*, 114101.
- [48] Y. Garsany, O. A. Baturina, K. E. Swider-Lyons, S. S. Kocha, *Anal. Chem.* **2010**, *82*, 6321–6328.

Manuscript received: March 8, 2023  
Revised manuscript received: May 10, 2023  
Version of record online: July 14, 2023